Multipermeability Inductors for Increasing the Inductance and Improving the Efficiency of High-Frequency DC/DC Converters

Laili Wang, *Member, IEEE*, Zhiyuan Hu, Yan-Fei Liu, *Fellow, IEEE*, Yunqing Pei, *Member, IEEE*, and Xu Yang, *Member, IEEE*

***Abstract*—Distributed air-gap inductors such as iron powder chip inductors and low-temperature cofired ceramic (LTCC) inductors have the advantage of low-fringing effect loss. However, the flux density nonuniformly distributes in the magnetic cores, which results in the magnetic material closer to the conductor becoming saturated while the magnetic material further away from the conductor is still not fully utilized. This paper proposes a multipermeability distributed air-gap inductor structure to increase inductance without the necessity of increasing the inductor volume. The best discrete permeability value is investigated. Based on the best discrete permeability value, inductance as well as the inductance density trends is calculated by varying the number of permeability layers under the condition that thickness for each layer is constant. Also, the inductance variations versus the number of permeability layers are also obtained under the condition that the inductor thickness is constant. A three-permeability inductor and a single-permeability inductor are fabricated to evaluate the proposed method. The measured results show that the three-permeability inductor has a much higher inductance than the single-permeability inductor for the entire load range. Both inductors are tested in a 5-V input, 3-V output dc/dc converter to compare their performances. The results show that the three-permeability inductor can further improve the efficiency of high-frequency dc/dc converters.**

***Index Terms*—Distributed air-gap, fringing effect, high efficiency, multipermeability.**

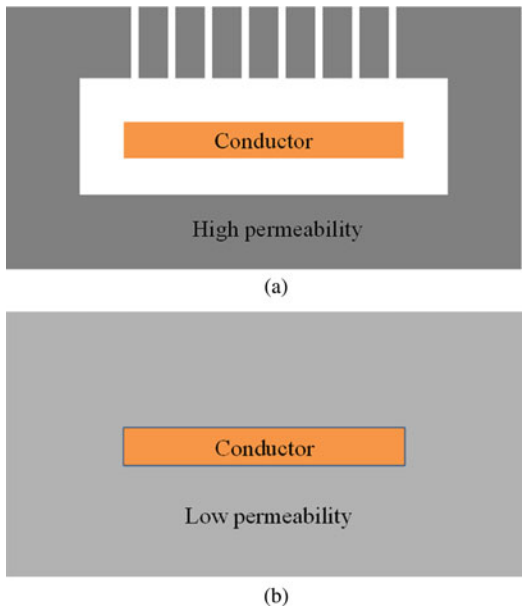

Fig. 1. Cross-sectional view of quasidistributed air-gap inductor and distributed air-gap inductor. (a) Quasidistributed air-gap. (b) Distributed air-gap inductor based on LTCC or thin film technology.

I. Introduction

THE inductor design for high-frequency dc/dc converters has been a very popular topic in recent years because it plays an important role in increasing the power density and in improving the efficiency. In conventional high-frequency dc/dc converters, the inductors are usually constructed with high permeability commercial magnetic cores and copper wires. For these inductors, air-gaps are needed to prevent the magnetic cores from going into saturation. However, in some applications such as voltage regulator modules (VRMs), the air-gap inductors are driven by an excitation containing a large amplitude ac excursion, causing serious eddy current conduction loss that can be produced by the leakage flux, known as fringing effect loss, resulting in a reduction of the converter efficiency [1]. Especially, as the new technologies drive the switching frequency of the converters higher, the size and the winding window of the magnetic cores become smaller and smaller; the windings are thus closely exposed to the high-frequency leakage flux. This causes the fringing effect loss to be higher, and it even becomes a major component of the total inductor loss. With the purpose of reducing the fringing effect loss, quasidistributed air-gap [2]–[5] and distributed air-gap [6]–[20] techniques have been proposed, as shown in Fig. 1. A quasidistributed air-gap inductor is modified from an air-gap inductor by dividing a large air-gap into some small gaps so that the fringing effect loss can be reduced. To further reduce the fringing effect loss, the distributed air-gap inductors, which are essentially equivalent to dividing the air-gap into a finite number of small gaps, have also been proposed in [8]–[26], [27]–[29]. Iron powder chip

Manuscript received May 25, 2012; revised August 16, 2012 and October 25, 2012; accepted October 30, 2012. Date of current version February 15, 2013.

L. Wang, Z. Hu, and Y.-F. Liu are with the Department of Electrical and Computer Engineering, Queen's University, Kingston, ON K7L3N6, Canada (e-mail: l.l.wang@mail.xjtu.edu.cn; yanfei.liu@queensu.ca).

Y. Pei and X. Yang are with the Department of Electrical Engineering, Power Electronics and Renewable Energy Center, Xi'an Jiaotong University, Xi'an, Shaanxi 710049, China (e-mail: peiyq@mail.xjtu.edu.cn; yangxu@mail.xjtu.edu.cn).

Color versions of one or more of the figures in this paper are available online at http://ieeexplore.ieee.org.

Digital Object Identifier 10.1109/TPEL.2012.2228504

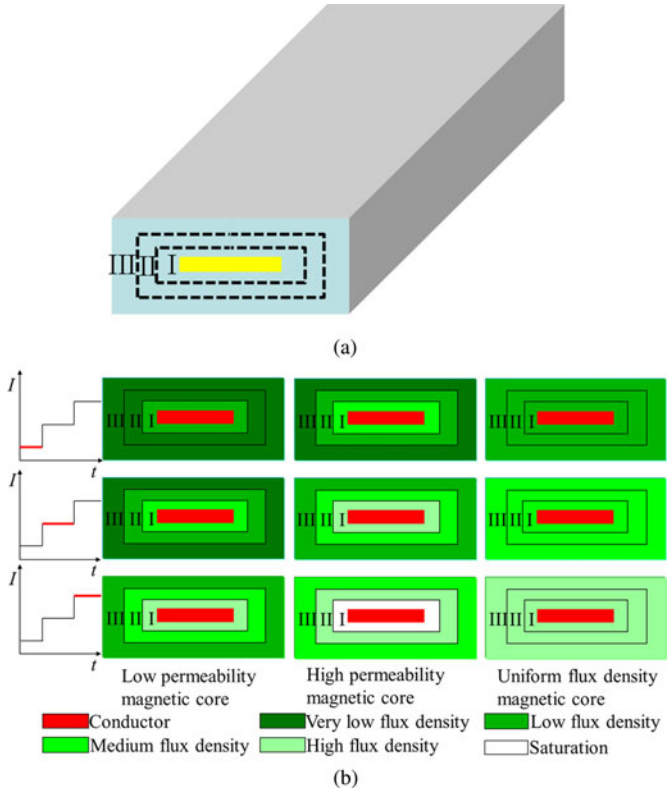

Fig. 2. Planar inductor and the flux-density distribution in it for different permeability configurations. (a) Structure of the inductor. (b) Flux-density distribution.

inductors and low-temperature cofired ceramic (LTCC) inductors are two typical examples. The iron power chip inductors have been widely used in industry while the LTCC inductors have become an increasingly popular topic in the academic research field [13]–[24], [27]. However, there is still a problem for designing such a distributed air-gap inductor since it has the disadvantage of nonuniform flux-density distribution in the magnetic cores. For air-gap inductors designed with commercial magnetic cores, the flux density in the core can be seen as uniform, but for distributed air-gap magnetic cores, the flux density in the magnetic cores can no longer be seen as uniform. It varies according to equivalent magnetic reluctance along the flux path. This inevitably leads to insufficient utilization of magnetic material. Fig. 2 roughly illustrates the flux-density distributions in three planar magnetic cores with the increase of current. The first magnetic core is made with lower permeability magnetic material, and the second one is made with higher permeability magnetic material. The cross sections of the both magnetic cores are roughly divided into three regions: Region I has the smallest magnetic reluctance, and Region III has the highest, while the Region II's magnetic reluctance is between them. For the first magnetic core, at full load, Region I has high flux density; Region II has medium flux density; and Region III has low flux density. However, at light load, Region II and Region III have very low flux density, which means that the magnetic material is not fully utilized. For the second magnetic core, under light- and medium-load conditions, the flux density of Region II and Region III is higher than that of the first magnetic core. However, at full load, Region I becomes saturated. It can be seen that the flux densities in both the low-permeability magnetic core and the high-permeability magnetic core are not uniform. The flux density of the outer side is much lower than that of the inner side. The nonuniform flux-density distribution is caused by the structure of the distributed air-gap inductors.

The utilization of the magnetic core is defined by the uniformity of the flux-density distribution in the magnetic core. When the flux density of the whole magnetic core reaches the allowed peak flux density (which is used in the traditional design of magnetics) simultaneously, the magnetic core is fully utilized. In the illustration above, the outer side as well as the magnetic material close to the outer side does not have the chance to make their flux density as high as the inner side. It turns out to be that part of the magnetic material cannot be fully utilized to explore its potential. In practice, there are many factors limiting the allowed peak flux density in the magnetic core, such as saturation, core loss, thermal limitation, and inductor size. However, whatever the allowed peak flux density is, the nonuniform flux distribution and utilization problem still exist for the distributed air-gap inductors, resulting in a low inductance value. To solve the problem, this paper proposes to improve the flux-density distribution in the magnetic core by gradually increasing the permeability from magnetic material closer to the conductor to further away from the conductor (Region I to Region III as shown in Fig. 2). As a result, the flux-density distribution shown in the uniform flux-density magnetic core is highly improved, and the inductance value can be significantly increased without increasing the volume.

Section II describes the principle of multipermeability inductors. Section III analyzes and optimizes the design of multipermeability distributed air-gap inductors based on theoretical calculation. Section IV presents the experimental results of a three-permeability inductor as well as a single-permeability inductor. Characteristics of the inductor prototypes are measured, and the inductors are evaluated in a dc/dc converter for comparison. Section V gives the conclusion.

II. Basic Idea of Multipermeability Inductors

This section introduces the basic idea and advantages of the multipermeability distributed air-gap inductors. Two typical kinds of distributed air-gap inductors are analyzed in this paper. One is toroidal inductors with circular cross section; the other one is planar inductors with square cross section. For the purpose of simplicity, this paper focuses on one turn inductors based on which multiple turns inductors can be designed. Fig. 3 shows the structures of the inductors. Their cross sections are shown in Fig. 4. Generally, the flux density in the single-permeability magnetic core can be expressed by

$$B_r = \frac{\mu_r \mu_0 I}{l_r} \tag{1}$$

where l_r is the length of the magnetic path, B_r is the corresponding flux density along the path, μ_0 is the permeability of air, and μ_r is the relative permeability of the magnetic material.

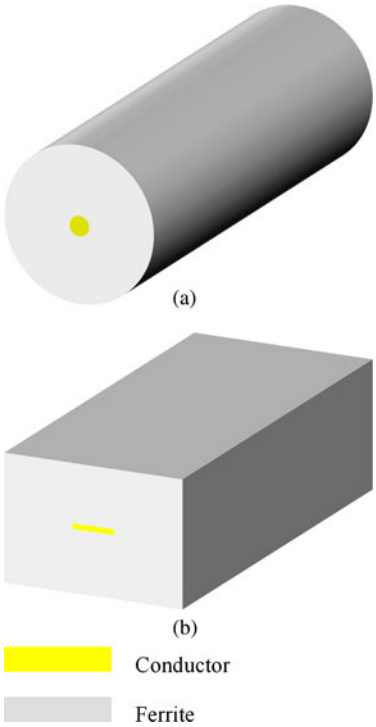

Fig. 3. One turn distributed air-gap inductors. (a) Toroidal inductor. (b) Planar inductor.

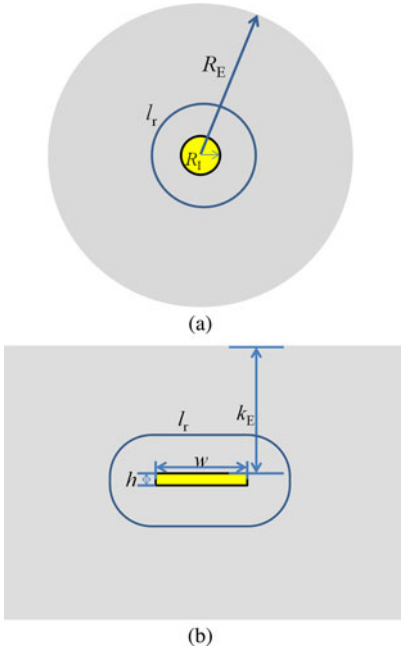

Fig. 4. Cross-sectional views of single permeability inductors. (a) Circular. (b) Square.

From the inner side to the outer side of the magnetic core, B_r gradually decreases as l_r gradually increases, which causes the nonuniform distribution of flux density. Fig. 5 shows the flux-density distribution of the two magnetic cores under 15 A excitation. The nonuniform flux-density distribution can be clearly observed. The flux density, which is far away from the conductor, is still very low while the flux density close to the

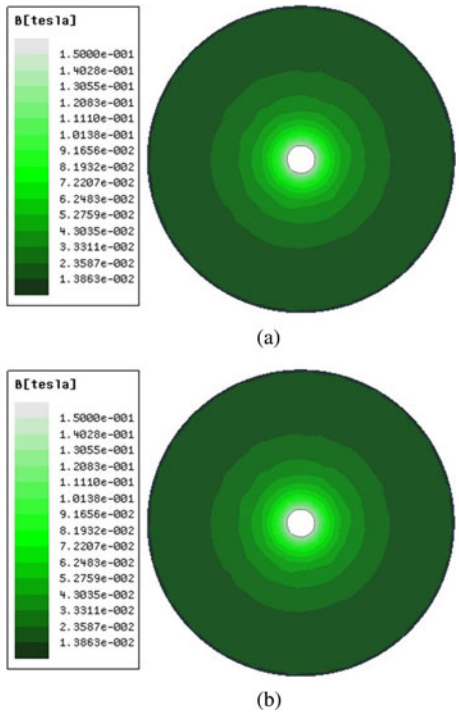

Fig. 5. Flux-density distribution in single-permeability distributed air-gap inductors. (a) Circular ($R_0 = 1$ mm). (b) Square ($w = 3$ mm, $h = 0.2$ mm).

conductor has reached its allowed peak value $B_{a\_\max}$. This means that the magnetic material is not fully utilized, leading to a low inductance value. By increasing the relative permeability of the magnetic material continuously from the inner side to the outer side of the magnetic core according to (2), uniform flux-density distribution can be achieved. The structures of the continuously changing permeability magnetic cores are shown in Fig. 6. Based on this method, the magnetic material can be fully utilized and the inductance value can be increased compared with the single-permeability inductors of the same volume

$$\mu_r(l_r) = \frac{B_{a\_\max} l_r}{\mu_0 I_f}. \tag{2}$$

The length of the magnetic path for the circular cross section can be expressed by its circumference

$$l_{r\_\text{circular}} = 2\pi r \tag{3}$$

where r is the radius of the circular magnetic path.

Since the distributed air-gap inductor in this paper is used to reduce the fringing effect loss caused by ac flux excursion, the inductance value should be calculated by dividing the flux variation with current variation as expressed by

$$L = \frac{\Delta\varphi}{\Delta I}. \tag{4}$$

The per unit length (1 m) inductance for a toroidal inductor can thus be expressed by

$$L_{c\_\text{circular}} = \int_{R_I}^{R_E} \frac{\mu_r(l_r)\mu_0}{l_{r\_\text{circular}}} dr. \tag{5}$$

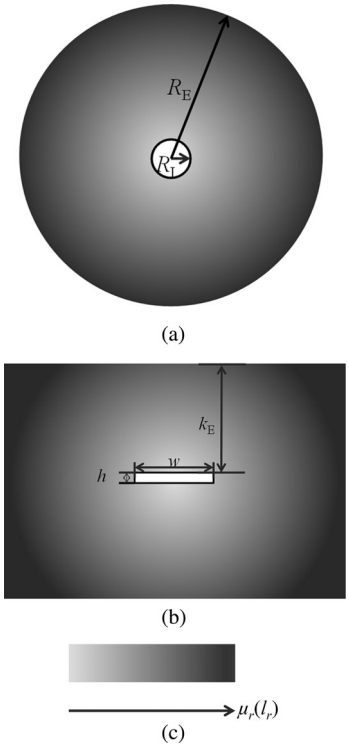

Fig. 6. Continuously changing permeability distribution in distributed air-gap inductors. (a) Circular. (b) Square.

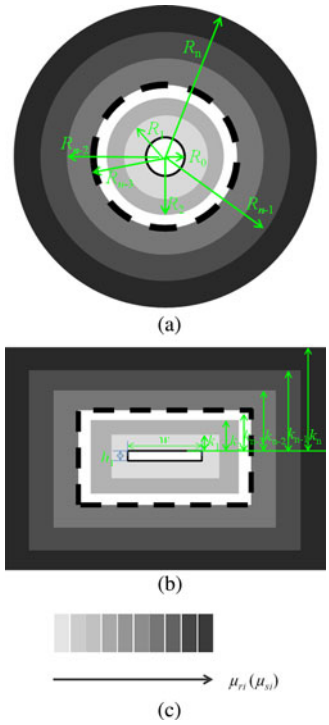

Fig. 7. Discrete permeability distribution in distributed air-gap inductors. (a) Circular. (b) Square.

The length of the magnetic path of the planar inductors can be expressed by the rectangle. Its length of the magnetic path can be expressed by

$$l_{r\_\text{square}} = 2(w+h) + 8k. \tag{6}$$

The per unit length inductance for a planar inductor can be expressed by

$$L_{c\_\text{square}} = \int_0^k \frac{\mu_r(l_r)\mu_0}{l_{r\_\text{square}}} dr. \tag{7}$$

With such a continuously changing permeability distribution, the whole magnetic core can reach the allowed peak flux density simultaneously; thus, the magnetic core is fully utilized. However, it is difficult to fabricate such a continuously changing permeability inductor in practice. Instead, we can divide the region of varying permeability into different small regions, and each small region has a discrete permeability. By doing this, a magnetic core whose permeability discretely changes can be realized. The inductors designed with these types of magnetic cores are named multipermeability inductors. Fig. 7 shows the structures of magnetic cores with n-layer multipermeability ferrites. Compared with the single-permeability structure, the proposed magnetic cores have discretely increasing permeability with the increase of radius or height. When the flux density in the magnetic core is lower than the allowed peak flux density, the permeability for toroidal and planar inductors can be expressed by

$$\mu_{ri}(r) = \begin{cases} \mu_{r1} & R_0 \le R < R_1 \\ \cdots & \cdots \\ \mu_{rn-1} & R_{n-2} < R < R_{n-1} \\ \mu_{rn} & R_{n-1} < R < R_n \end{cases} \tag{8}$$

$$\mu_{si}(r) = \begin{cases} \mu_{s1} & k_0 \le k < k_1 (k_0 = 0) \\ \cdots & \cdots \\ \mu_{sn-1} & k_{n-2} < k < k_{n-1} \\ \mu_{sn} & k_{n-1} < k < k_n. \end{cases} \tag{9}$$

And the per unit length inductance can be expressed by

$$L_{d\_\text{circular}} = \sum_{i=1}^{n} \int_{R_{i-1}}^{R_i} \frac{\mu_{ri}\mu_0}{l_{r\_\text{circular}}} dr \tag{10}$$

$$L_{d\_\text{square}} = \sum_{i=1}^{n} \int_{k_{i-1}}^{k_i} \frac{\mu_{\text{si}}\mu_0}{l_{r\_\text{square}}} dr. \tag{11}$$

III. Design of Multipermeability Inductors

In this section, four parameters are further analyzed for the optimal design of the toroidal and planar multipermeability inductors. They are the permeability values, the thickness of each permeability layer, the radius or height of the inductors, and the number of permeability layers. For the purpose of quantitative analysis, assumptions about the BH curve have to be made. Fig. 8 shows the assumptive BH curves.

1) To simplify the calculation of inductance, the nonlinear BH curve is approximated by a piecewise linear BH curve. The first segment ends at the allowed peak flux density.

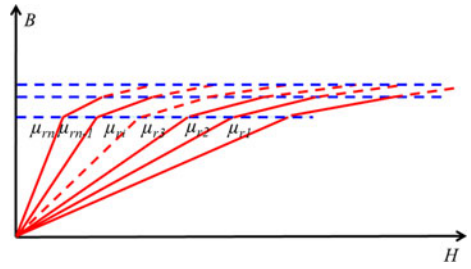

Fig. 8. Idealistic BH curve under the assumptions.

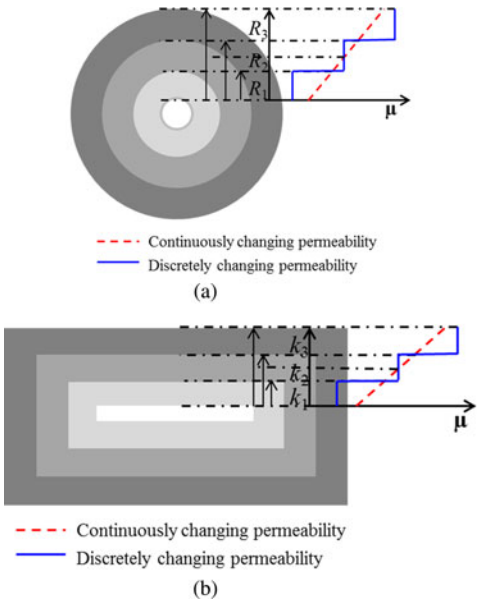

Fig. 9. Two three-permeability inductors and the permeability distributions. (a) Circular. (b) Square.

2) The permeability of the following segment is approximately one quarter of the previous segment based on the nonlinear BH curve.
3) All the magnetic materials have the same allowed peak flux density even though their saturation flux density maybe different.

A. *Permeability Distribution*

Two three-permeability magnetic cores are taken as examples to illustrate the typical permeability distributions in a multipermeability inductor. The magnetic cores and their permeability distributions are shown in Fig. 9. The dashed line shows the permeability versus radius for a continuously changing permeability distribution obtained according to (2). As the flux density in (2) is chosen to be the allowed peak flux density, permeability obtained through (2) should be the permeability defined in (8) and (9). There are three cases for choosing discrete permeability. The first one is that discrete permeability is lower than the continuous permeability in the radius or height range $R < R_1$ $(k < k_1)$; the second case is that discrete permeability is higher than one part of continuous permeability, but lower than the other part in the radius range $R_1 < R < R_2$ $(k_1 < k < k_2)$; the third case is that discrete permeability is completely higher

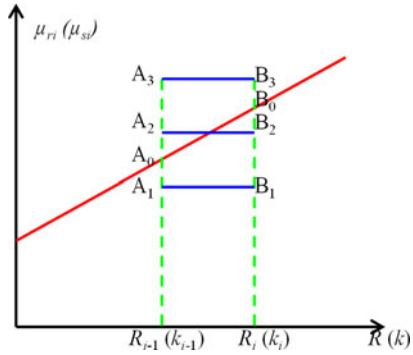

Fig. 10. Three cases of discrete permeability distributions.

than the continuous permeability in the range $R_2 < R < R_3$ $(k_2 < k < k_3)$. For the first case, the inductance contributed by this permeability is lower than the inductance from a continuous permeability distribution, but the permeability will be effective through the whole load range. For the second case, the first part of the magnetic material will have a flux density higher than the allowed peak flux density at full load, and its permeability value then becomes one quarter of the original value. But the flux density of the second part is still lower than the allowed peak flux density, and the permeability, thus, does not change. For the third case, the discrete permeability is completely higher than the continuous permeability; thus, its permeability equals one quarter of the original value, and has less of a contribution for the total inductance at full load. (Flux density reaching the second segment is only analyzed here, but for higher flux density which reaches the higher order segments, the conclusion will be the same.)

An analysis is conducted to show the effect of the three typical permeability distributions to inductance values for a specific magnetic material. Fig. 10 shows the three permeability distributions for the magnetic material between R_{i-1} (k_{i-1}) and R_i (k_i). A_0B_0 is the continuous permeability curve between R_{i-1} (k_{i-1}) and R_i (k_i). A_1B_1 and A_3B_3 show permeability distributions, which are lower and higher than the continuous permeability, respectively. A_2B_2 shows the discrete permeability crossing the continuous permeability curve.

The permeability at A_0 and B_0 can be calculated for both kinds of inductors. Per unit length inductances versus current will be analyzed separately for the three cases.

For circular shape

$$\mu_r(A_0) = \frac{B_{a\_\max} 2\pi R_{i-1}}{\mu_0 I_f} \tag{12}$$

$$\mu_r(B_0) = \frac{B_{a\_\max} 2\pi R_i}{\mu_0 I_f}. \tag{13}$$

For square shape

$$\mu_s(A_0) = \frac{2B_{a\_\max}(w + h + 4k_{i-1})}{\mu_0 I_f} \tag{14}$$

$$\mu_s(B_0) = \frac{2B_{a\_\max}(w + h + 4k_i)}{\mu_0 I_f}. \tag{15}$$

1) First Case (A_1B_1)*:* The permeability at point A_1 is lower than the continuous permeability as shown in (16) or (17); therefore, the flux density of point A_1 is lower than $B_{a\_\max}$ for the whole load range; the inductance of toroidal inductor and the inductance of planar inductor can be easily expressed by (18) and (19), respectively

$$\mu_r(A_1) < \mu_r(A_0) \tag{16}$$

$$\mu_s(A_1) < \mu_s(A_0) \tag{17}$$

$$L_{d\_\mathrm{circular}\_A_1B_1} = \frac{\mu_r(A_1)\mu_0}{2\pi}\ln\left(\frac{R_i}{R_{i-1}}\right) \tag{18}$$

$$L_{d\_\mathrm{square}\_A_1B_1} = \frac{\mu_s(A_1)\mu_0}{8}\ln\left(\frac{w+h+4k_i}{w+h+4k_{i-1}}\right). \tag{19}$$

2) Second Case (A_2B_2)*:* The permeability at point A_2 is higher than that at point A_0 while the permeability at point B_2 is still lower than that at point B_0 as shown in (20) and (21). This means that the flux density does not surpass the allowed peak flux density when (22) and (23) are satisfied, and the inductance of a toroidal inductor and the inductance of a planar inductor can be expressed by (24) and (25), respectively. However, when the current further increases, (26) and (27) become satisfied, and the flux density begins to surpass the allowed flux density from R_{i-1} (k_{i-1}); the inductances then can be expressed by (28) and (29), respectively

$$\mu_r(A_0) < \mu_r(A_2) < \mu_r(B_0) \tag{20}$$

$$\mu_s(A_0) < \mu_s(A_2) < \mu_s(B_0) \tag{21}$$

$$I < \frac{\mu_r(A_0)}{\mu_r(A_2)}I_f \tag{22}$$

$$I < \frac{\mu_s(A_0)}{\mu_s(A_2)}I_f \tag{23}$$

$$L_{d\_\mathrm{circular}\_A_2B_2} = \frac{\mu_r(A_2)\mu_0}{2\pi}\ln\left(\frac{R_i}{R_{i-1}}\right) \tag{24}$$

$$L_{d\_\mathrm{square}\_A_2B_2} = \frac{\mu_s(A_2)\mu_0}{8}\ln\left(\frac{w+h+4k_i}{w+h+4k_{i-1}}\right) \tag{25}$$

$$\frac{\mu_r(A_0)}{\mu_r(A_2)}I_f \le I \le I_f \tag{26}$$

$$\frac{\mu_s(A_0)}{\mu_s(A_2)}I_f \le I \le I_f \tag{27}$$

$$L_{d\_\mathrm{circular}\_A_2B_2} = \frac{\mu_r(A_2)\mu_0}{8\pi} \times \ln\left(\frac{R_{i-1}+\frac{\mu_r(A_2)I-\mu_r(A_0)I_f}{(\mu_r(B_0)-\mu_r(A_0))I_f}(R_i-R_{i-1})}{R_{i-1}}\right) + \frac{\mu_r(A_2)\mu_0}{2\pi} \times \ln\left(\frac{R_i}{R_{i-1}+\frac{\mu_r(A_2)I-\mu_r(A_0)I_f}{(\mu_r(B_0)-\mu_r(A_0))I_f}(R_i-R_{i-1})}\right) \tag{28}$$

$$L_{d\_\mathrm{square}\_A_2B_2} = \frac{\mu_s(A_2)\mu_0}{32} \times \ln\left(\frac{w+h+4k_{i-1}+\frac{\mu_s(A_2)I-\mu_s(A_0)I_f}{(\mu_s(B_0)-\mu_s(A_0))I_f}(k_i-k_{i-1})}{w+h+4k_i}\right) + \frac{\mu_s(A_2)\mu_0}{8} \times \ln\left(\frac{w+h+4k_i}{w+h+4k_{i-1}+\frac{\mu_s(A_2)I-\mu_s(A_0)I_f}{(\mu_s(B_0)-\mu_s(A_0))I_f}(k_i-k_{i-1})}\right). \tag{29}$$

3) Third Case (A_3B_3)*:* The permeability at point A_3 is higher than that at point B_0 as shown in (30) and (31). Therefore, the inductance calculation can be divided into three stages as the current gradually increases. When (32) and (33) are satisfied, the inductance of the toroidal inductor and the inductance of the planar inductor can be expressed by (34) and (35), which are actually the same with the first case except that the permeability is higher. As the current further increases and (36) and (37) become satisfied, the flux density begins to surpass the allowed peak flux density $B_{a\_\max}$ from R_{i-1} (k_{i-1}), and the inductances can be expressed by (38) and (39), which are the same with the second stage of the second case except for the permeability. When the current reaches as high as expressed in (40) and (41), the flux density of magnetic core completely enters into the second segment, and then the inductance can be expressed by (42) and (43) respectively

$$\mu_r(A_3) > \mu_r(B_0) \tag{30}$$

$$\mu_s(A_3) > \mu_s(B_0) \tag{31}$$

$$I < \frac{\mu_r(A_0)}{\mu_r(A_3)}I_f \tag{32}$$

$$I < \frac{\mu_s(A_0)}{\mu_s(A_3)}I_f \tag{33}$$

$$L_{d\_\mathrm{circular}\_A_3B_3} = \frac{\mu_r(A_3)\mu_0}{2\pi}\ln\left(\frac{R_i}{R_{i-1}}\right) \tag{34}$$

$$L_{d\_\mathrm{square}\_A_3B_3} = \frac{\mu_s(A_3)\mu_0}{8}\ln\left(\frac{w+h+4k_i}{w+h+4k_{i-1}}\right) \tag{35}$$

$$\frac{\mu_r(A_0)}{\mu_r(A_3)}I_f \le I \le \frac{\mu_r(B_0)}{\mu_r(A_3)}I_f \tag{36}$$

$$\frac{\mu_s(A_0)}{\mu_s(A_3)}I_f \le I \le \frac{\mu_s(B_0)}{\mu_s(A_3)}I_f \tag{37}$$

$$L_{d\_\mathrm{circular}\_A_3B_3} = \frac{\mu_r(A_3)\mu_0}{8\pi} \times \ln\left(\frac{R_{i-1}+\frac{\mu_r(A_3)I-\mu_r(A_0)I_f}{(\mu_r(B_0)-\mu_r(A_0))I_f}(R_i-R_{i-1})}{R_{i-1}}\right) + \frac{\mu_r(A_3)\mu_0}{2\pi} \times \ln\left(\frac{R_i}{R_{i-1}+\frac{\mu_r(A_3)I-\mu_r(A_0)I_f}{(\mu_r(B_0)-\mu_r(A_0))I_f}(R_i-R_{i-1})}\right) \tag{38}$$

$$L_{d\_\text{square}\_A_3B_3} = \frac{\mu_s(A_3)\mu_0}{32} \times \ln\left(\frac{w+h+4(k_{i-1}+\frac{\mu_s(A_3)I-\mu_s(A_0)I_f}{(\mu_s(B_0)-\mu_s(A_0))I_f}(k_i-k_{i-1}))}{w+h+4k_{i-1}}\right) + \frac{\mu_s(A_3)\mu_0}{8} \times \ln\left(\frac{w+h+4k_i}{w+h+4(k_{i-1}+\frac{\mu_s(A_3)I-\mu_s(A_0)I_f}{(\mu_s(B_0)-\mu_s(A_0))I_f}(k_i-k_{i-1}))}\right) \tag{39}$$

$$I > \frac{\mu_r(B_0)}{\mu_r(A_3)} I_f \tag{40}$$

$$I > \frac{\mu_s(B_0)}{\mu_s(A_3)} I_f \tag{41}$$

$$L_{d\_\text{circular}\_A_3B_3} = \frac{\mu_r(A_3)\mu_0}{8\pi} \ln\left(\frac{R_i}{R_{i-1}}\right) \tag{42}$$

$$L_{d\_\text{square}\_A_3B_3} = \frac{\mu_r(A_3)\mu_0}{32} \ln\left(\frac{w+h+4k_i}{w+h+4k_{i-1}}\right). \tag{43}$$

Based on the aforementioned analysis, the inductances versus the current for the three cases are illustrated in Fig. 11. For case 1, the inductances keep constant for the whole load range, but they have the lowest inductance at light load. For cases 2 and 3, the permeability is higher; thus, the inductances at light load are higher, but they have inductance drops near the full load, showing great nonlinearity. The nonlinear inductance makes the response to voltage drops and current transients also have great nonlinearity, which can create difficulties with designing circuits and problems with possible feedback. For this reason, the permeability at R_{i-1} (k_{i-1}) should not be higher than the continuous permeability at Point A_0, which is $\mu_r(A_0)$ or $\mu_s(A_0)$ to ensure that there is no inductance nonlinearity. However, the magnetic material still cannot be utilized fully if the permeability is lower than $\mu_r(A_0)$ or $\mu_s(A_0)$ as in the first case. Therefore, to increase the inductance as much as possible, the highest permeability for the magnetic material between R_{i-1} (k_{i-1}) and R_i (k_i) is $\mu_r(A_0)$ $(\mu_s(A_0))$.

B. Radius or Height of an Inductor With Constant Permeability Layer Thickness

As analyzed previously, discrete permeability should equal to the continuous permeability at R_{i-1} (k_{i-1}) so that each ferrite layer can be fully utilized. The next question is how to design the thickness for each layer to maximize the total inductance if the total number of layers and the total thickness of the magnetic core have been given. Based on comprehensive analytical calculations, as shown in Fig. 12, it turns out that an even permeability discretization and an equal thickness for all the permeability layers are very close to the optimum solution. This section further discusses the advantage of the inductance value increase effect of the multipermeability inductor compared with the low single-permeability structure under the condition that

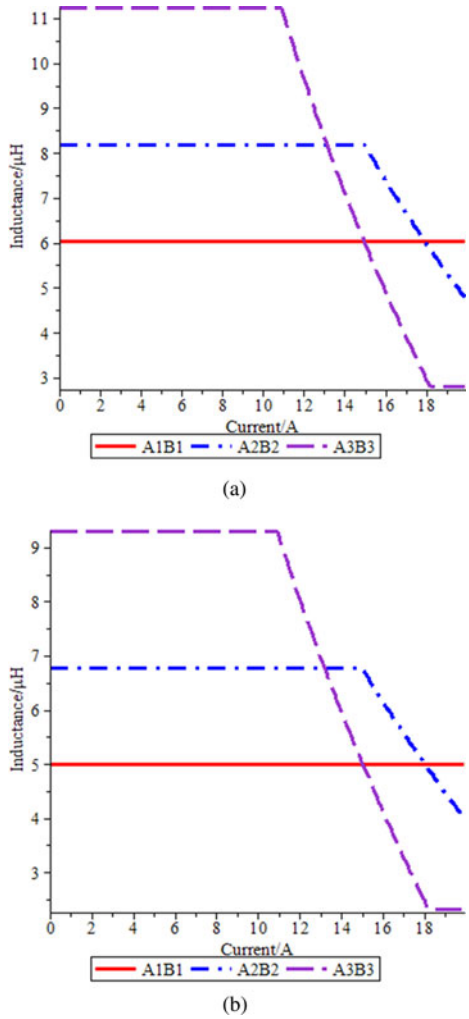

Fig. 11. Per unit length inductance versus current for different permeability configurations. (a) Circular. (b) Square.

they have the same size (it can also be seen that the multipermeability inductor has a smaller size under the condition that they have the same inductance). Fig. 13 shows the per unit length inductance of the two kinds of inductors versus the inductor radius and height when the thickness of each permeability layer is the same. The inductance of the multipermeability inductor increases proportionally to the total radius or height while the inductance increase of a single- permeability inductor becomes smaller and smaller as the radius or height increases. It is obvious that for a multipermeability inductor, the larger the radius or height, the more significant the increase of inductance increase. The inductance densities (obtained by dividing the inductance with inductor volume) of the same volume magnetic cores with the three kinds of permeability configurations are illustrated in Fig. 14. It can be observed that although the inductance of the multipermeability inductor is a little bit less than that of the continuously changing permeability inductor, it is much higher than that of the single-permeability inductor. A simulation is also set up to show the flux-density distribution of multipermeability inductors. The results are shown in Fig. 15. Compared with the single-permeability magnetic cores in Fig. 5, the

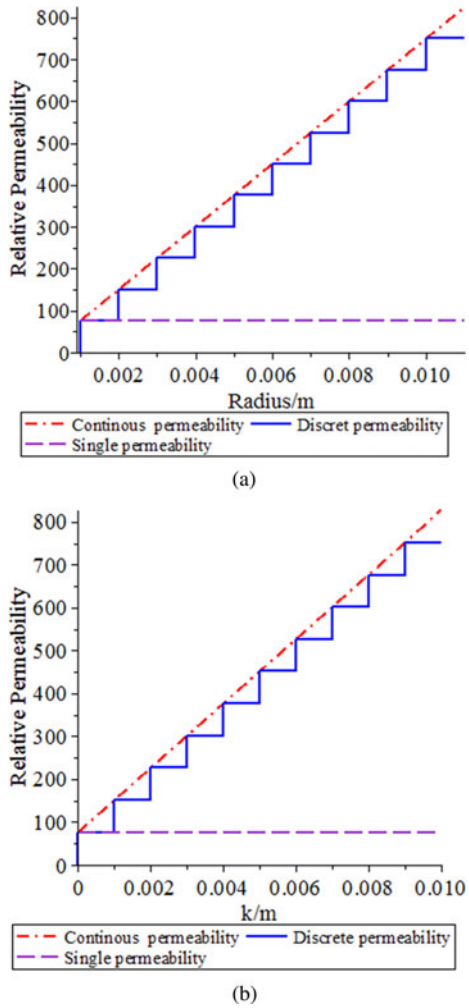

Fig. 12. Permeability versus radius or height. (a) Circular ($R_0 = 1$ mm). (b) Square ($w = 3$ mm, $h = 0.2$ mm).

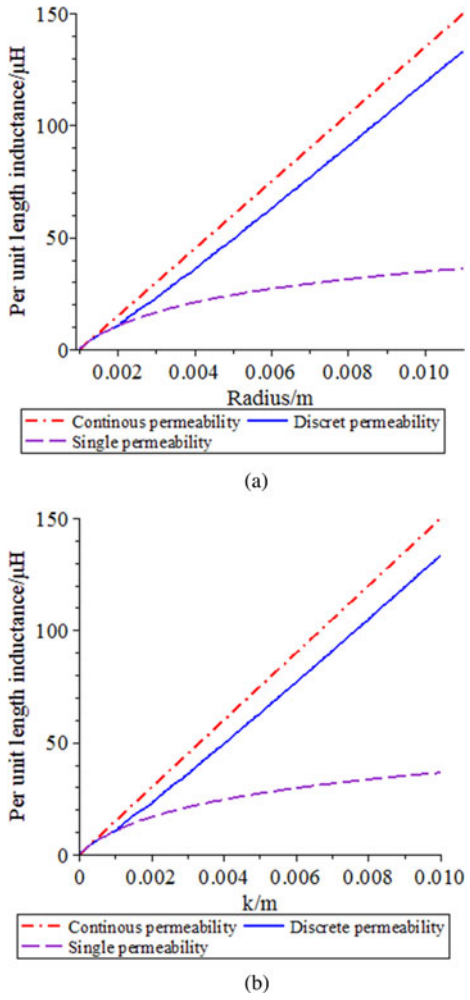

Fig. 13. Per unit length inductance versus radius or height. (a) Circular ($R_0 = 1$ mm). (b) Square ($w = 3$ mm, $h = 0.2$ mm).

multipermeability magnetic cores have much more uniform high-flux distribution, which allows the whole cores to be fully utilized.

C. Number of Permeability Layers of an Inductor With a Constant Radius or Height

Another factor that influences the inductance value is the number of permeability layers in the magnetic core. A multipermeability structure is essentially an intermediate state between a single-permeability structure and a continuously changing permeability structure, which can be seen as a multipermeability structure with an infinite number of permeabilities. To illustrate the impact of the number of permeability layers on inductance, a calculation is made in this section to show the inductance value versus the number of permeability layers. Fig. 16 shows the discrete inductance values with the number of permeability layers. As the number of permeability layers gradually increases from 1 to 50, the inductance for the toroidal inductor increases from 39 to 59 μH (for square cross section, the inductance increases from 26 to 70 μH). And the inductances become closer and closer to the inductances of the inductors formed with continuously changing permeability magnetic cores. Considering the inductance value gain and complexity of the manufacturing process, it is suggested that three to ten layers are used for general design.

IV. Prototype Fabrication and Experiment

To identify the inductance increasing effect of the multipermeability inductors, a three-permeability inductor is fabricated in this section. For the purpose of comparison, a single-permeability inductor is also fabricated. The two inductors have the same volume, which is 2.47 cm^3 and the same length, which is 3 cm. Their pictures are shown in Fig. 17. The cross-sectional views are shown in Fig. 18. The windings for both single-permeability and three-permeability inductors are copper wires with 1-mm radius. Three kinds of the ferrite sheets are selected to make the magnetic cores. They are C350 from Epcos, and IRJ04 and IRJ09 from TDK. They have a relative permeability of 9, 40, and 100, respectively. The three-permeability inductor is designed by using C305 as the inner layer, IRJ04 as the middle layer, and IRJ09 as the outer layer. Due to the lack of available magnetic sheets with the desired permeability, the thickness for

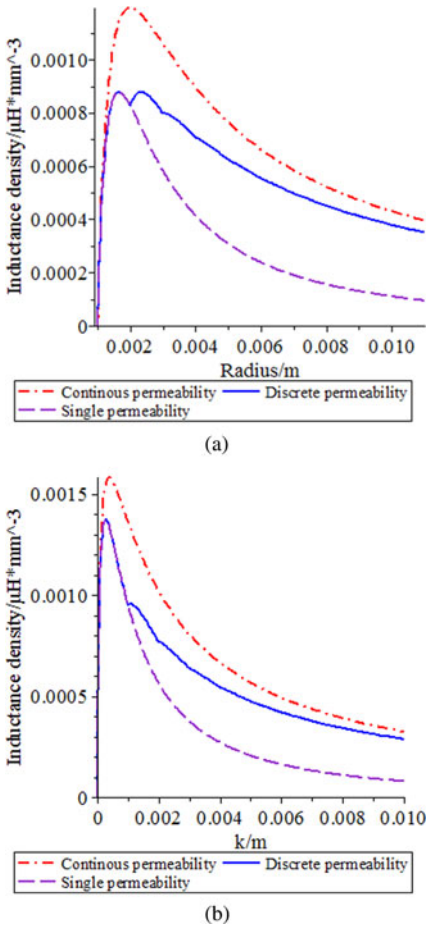

Fig. 14. Inductance density versus radius or height. (a) Circular ($R_0 = 1$ mm). (b) Square ($w = 3$ mm, $h = 0.2$ mm).

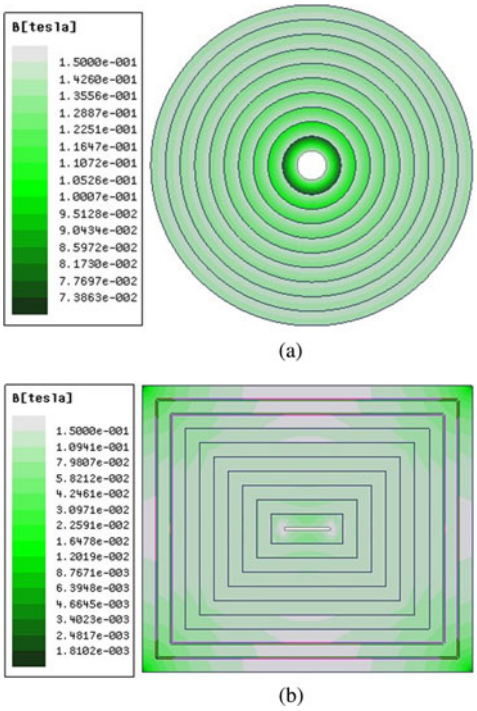

Fig. 15. Flux-density distribution of multipermeability inductors. (a) Circular ($R_0 = 1$ mm). (b) Square ($w = 3$ mm, $h = 0.2$ mm).

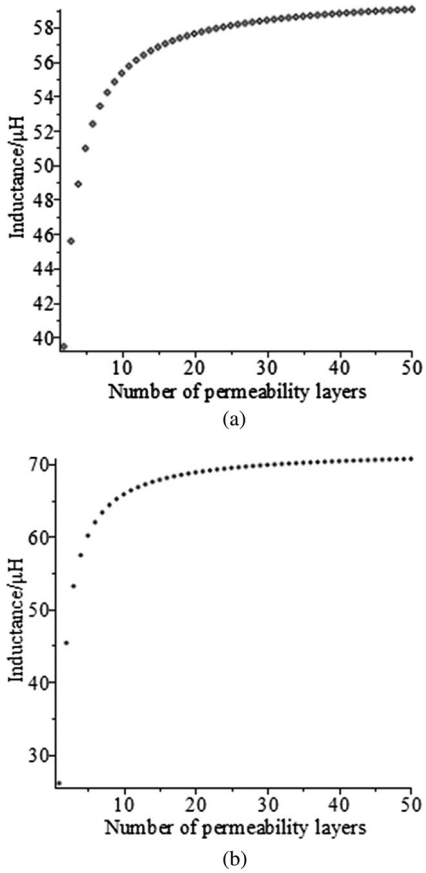

Fig. 16. Inductance values versus number of permeability. (a) Circular ($R_0 = 1$ mm, $R_n = 5$ mm). (b) Square ($w = 3$ mm, $h = 0.1$ mm, $k_1 = 0.2$ mm, $k_n = 5$ mm).

Fig. 17. Pictures of the inductor prototypes.

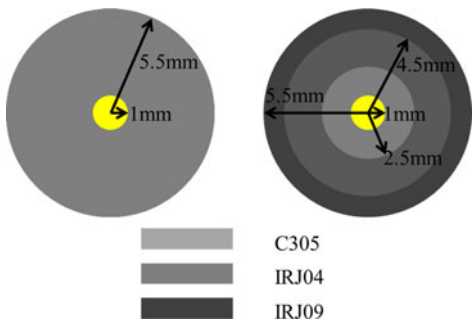

Fig. 18. Cross-sectional views of the single-permeability inductor and three-permeability inductor.

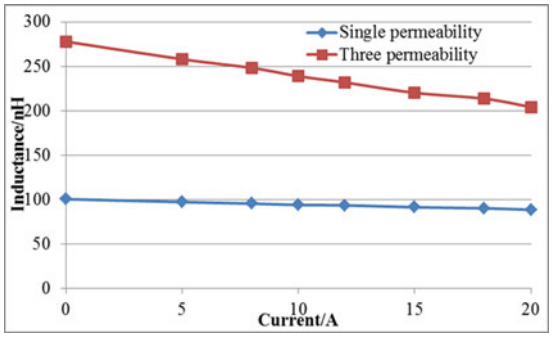

Fig. 19. Inductance versus current.

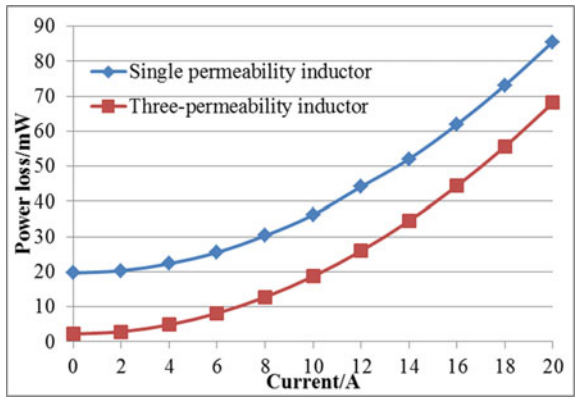

Fig. 20. Winding loss of the single-permeability inductor and the three-permeability inductor.

each kind of permeability cannot be designed to be the same. To ensure that the winding resistance is low enough, the radius of the conductor is selected to be 1 mm, and the inner radius of the first magnetic layer is, thus, 1 mm. The inner radii of the other two magnetic layers are determined by

$$R_{\text{in}} = \frac{\mu_r \mu_0 I_f}{2\pi B_{a\_\max}} \tag{44}$$

where $B_{a\_\max}$ is the allowed peak flux density of magnetic material; I_f is the full-load capability; and μ_r is the relative permeability. The radius of the outer layer is 5.5 mm, which is actually determined by the whole inductor volume. Based on previous calculated radius values, the thickness of each magnetic layer could be easily obtained; they are 1.5, 2, and 1 mm, respectively.

A 1 MHz 5-V input 3-V output buck converter is constructed to test the two inductor prototypes. The two inductors are applied in the converter to obtain their inductances versus current curve by measuring the peak–peak current ripple. The results are shown in Fig. 19. The single-permeability inductor has a nearly constant inductance for the whole load range, which is 100 nH. For the three-permeability inductor, the light-load inductance is 280 nH, which is almost three times the single-permeability inductor, but it gradually drops to 200 nH due to the nonlinear characteristic of the BH curve. Finite element analysis (FEA) software is used to simulate the winding loss with the purpose of evaluating the loss of the two inductor prototypes in the converter. The result is shown in Fig. 20. Benefiting from its higher inductance value and lower current ripple, the three-permeability inductor has about 20 mW lower winding loss than the single-permeability inductor does although the winding losses of both inductors are not more than 90 mW (the loss on the connection between inductor and the PCB board is not taken into account). For the lack of the Steinmetz parameters of the magnetic materials, the core loss of the two inductors cannot be obtained by simulation. However, their thermal pictures under the same operating condition are taken to compare the core loss indirectly. Fig. 21 shows the thermal pictures of the two inductors. It can be observed that the three-permeability inductor has nearly the same temperature as the single-permeability inductor, which means that the core loss is at least not significantly increased by adding higher permeability magnetic materials. The efficiencies of the converter with the two inductors are also

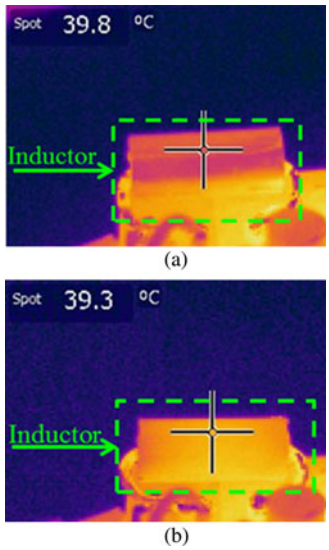

Fig. 21. Thermal pictures of the inductors in the tested dc/dc converter. (a) Single permeability inductor. (b) Three-permeability inductor.

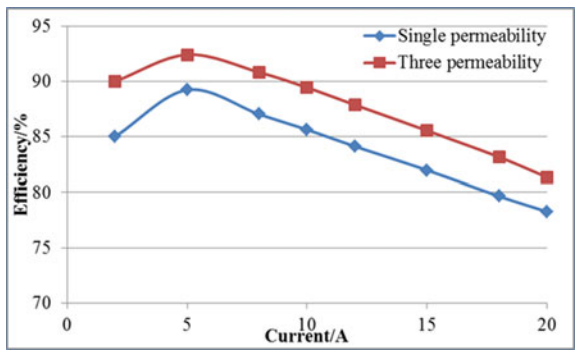

Fig. 22. Efficiency versus current.

tested to show the effect of efficiency improvement of multipermeability inductors for its higher inductance leading to lower current ripple. The results are shown in Fig. 22. The efficiency of the converter with the three-permeability inductor is about 4% higher than that of the single- permeability inductor, which means that the multipermeability inductor can help to improve the efficiency of the converters due to the inductance increase.

V. Conclusion

This paper proposed a multipermeability inductor structure to improve nonuniformly distributed flux density of distributed air-gap inductors. Analysis shows that the inductance value can be significantly increased based on this structure. The permeability values, the radius and height of the inductor, and the number of permeability layers are analyzed to optimize the design of a multipermeability inductor. The most effective permeability for each layer of ferrites is to make them equal to the corresponding continuous permeability at the inner radius or height. If the thickness of each layer is constant, then the inductance can be significantly increased when the number of permeability layers as well as the inductor radius or thickness is increased. Increasing the number of discrete permeability layers can also increase the inductance value when the inductor radius or height is constant, but the effect is less and less significant as the number of discrete permeability layers becomes larger. To identify the inductance increase effect, a three-permeability inductor and a single-permeability inductor of the same volume are made for comparison. The single-permeability inductor has a nearly constant inductance of 100 nH for the whole load range while the three-permeability inductor has a 280 nH inductance at light load and a 200 nH inductance at full load. Compared with the single-permeability inductor, the three-permeability inductor can improve the efficiency of a dc/dc converter by 4%.

References

[1] K. D. T. Ngo and M. H. Kuo, "Effects of air gaps on winding loss in high-frequency planar magnetics," in *Proc. IEEE Power Electron. Spec. Conf.*, 1988, vol. 2, pp. 1112–1119.

[2] W. M. Chew, P. D. Evans, and W. J. Heffernan, "High frequency inductor design concepts," in *Proc. IEEE Power Electron. Spec. Conf.*, 1991, pp. 673–678.

[3] L. Daniel, C. R. Sullivan, and S. R. Sanders, "Design of microfabricated inductors," *IEEE Trans. Power Electron.*, vol. 14, no. 4, pp. 709–723, Jul. 1999.

[4] H. Jiankun and C. R. Sullivan, "AC resistance of planar power inductors and the quasidistributed gap technique," *IEEE Trans. Power Electron.*, vol. 16, no. 4, pp. 558–567, Jul. 2001.

[5] J. Wang, X. Yang, H. Niu, Z. Wang, and J. Liu, "PCB integrated transformer composed with ferrite mosaics for LLC resonant converter," in *Proc. IEEE Energy Convers. Congr. Expo.*, 2009, pp. 1032–1038.

[6] Q. Li, M. Lim, J. Sun, A. Ball, Y. Ying, F. C. Lee, and K. D. T. Ngo, "Technology road map for high frequency integrated DC-DC converter," in *Proc. IEEE Appl. Power Electron. Conf.*, 2010, pp. 533–539.

[7] S. Iyengar, T. M. Liakopoulos, and C. H. Ahn, "A DC/DC boost converter toward fully on-chip integration using new micromachined planar inductors," in *Proc. Power Electron. Spec. Conf.*, 1999, pp. 72–76.

[8] Y. Katayama, S. Sugahara, H. Nakazawa, and M. Edo, "High-power-density MHz-Switcing monolithic DC-DC converter with thin-film inductor," in *Proc. Power Electron. Spec. Conf.*, 2000, pp. 1485–1490.

[9] P. Dhagat, S. Prabhakaran, and C. R. Sullivan, "Comparison of magnetic materials for V-groove inductors in optimized high-frequency DC-DC converters," *IEEE Trans. Magn.*, vol. 40, no. 4, pp. 2008–2010, Jul. 2004.

[10] C. R. Sullivan and S. R. Sanders, "Design of microfabricated transformers and inductors for high-frequency power conversion," *IEEE Trans. Power Electron.*, vol. 11, no. 2, pp. 228–238, Mar. 1996.

[11] E. Waffenschmidt, B. Ackermann, and J. A. Ferreira, "Design method and material technologies for passives in printed circuit board embedded circuits," *IEEE Trans. Power Electron.*, vol. 20, no. 3, pp. 576–584, May 2005.

[12] M. Ludwig, M. Duffy, T. O'Donnell, P. McCloskey, and S. C. Ó Mathùna, "PCB Integrated inductors for low power DC/DC converter," *IEEE Trans. Power Electron.*, vol. 18, no. 4, pp. 937–945, Jul. 2003.

[13] C.-Y. Kim, H.-J. Kim, and J.-R. Kim, "An integrated LTCC inductor," *IEEE Trans. Magn.*, vol. 41, no. 14, pp. 3556–3558, Oct. 2005.

[14] H.-J. Kim, Y.-J. Kim, and J.-R. Kim, "An integrated LTCC inductor embedding NiZn ferrite," *IEEE Trans. Magn.*, vol. 42, no. 10, pp. 2840–2842, Oct. 2006.

[15] M. H. Lim, J. D. van Wyk, and Z. Liang, "Effect of geometry variation of LTCC distributed air-gap filter inductor on light load efficiency of DC-DC converters," in *Proc. IEEE Ind. Appl. Conf.*, 2006, pp. 1884–1890.

[16] M. H. Lim, Z. Liang, and J. D. van Wyk, "Low profile integratable inductor fabricated based on LTCC technology for microprocessor power delivery applications," *IEEE Trans. Compon. Packag. Technol.*, vol. 30, no. 1, pp. 170–177, Mar. 2007.

[17] M. H. Lim, J. D. van Wyk, F. C. Lee, and K. D. T. Ngo, "A class of ceramic-based chip inductors for hybrid integration in power supplies," *IEEE Trans. Power Electron.*, vol. 23, no. 3, pp. 1556–1564, May 2008.

[18] M. H. Lim, J. D. van Wyk, and F. C. Lee, "Hybrid integration of a low-voltage, high-current power supply buck converter with an LTCC substrate inductor," *IEEE Trans. Power Electron.*, vol. 25, no. 9, pp. 2287–2298, Sep. 2010.

[19] Q. Li, Y. Dong, and F. C. Lee, "High density low profile coupled inductor design for integrated Point-of-Load converter," in *Proc. IEEE Appl. Power Electron. Conf.*, 2010, pp. 79–85.

[20] M. Mu, Y. Su, Q. Li, and F. C. Lee, "Magnetic characterization of low temperature co-fired ceramic (LTCC) ferrite materials for high frequency power converters," in *Proc. IEEE Energy Convers. Congr. Expo.*, 2011, pp. 2133–2138.

[21] L. Wang, Y. Pei, X. Yang, X. Cui, and Z. Wang, "Three-dimensional integration of high frequency DC/DC converters based on LTCC technology," in *Proc. IEEE Power Electron. and Motion Control Conf.*, 2009, pp. 745–748.

[22] L. Wang, Y. Pei, X. Yang, and Z. Wang, "Design of ultrathin LTCC coupled inductors for compact DC/DC converters," *IEEE Trans. Power Electron.*, vol. 26, no. 9, pp. 2528–2541, Sep. 2011.

[23] L. Wang, Y. Pei, X. Yang, X. Cui, Z. Wang, and G. Zhao, "Design of multi-turn LTCC inductors for high frequency DC/DC converters," in *Proc. IEEE Appl. Power Electron. Conf.*, 2010, pp. 1610–1615.

[24] L. Wang, Y. Pei, X. Yang, Q. Yang, and Z. Wang, "Improving light and intermediate load efficiencies of buck converters with planar nonlinear inductors and variable on time control," *IEEE Trans. Power Electron.*, vol. 27, no. 1, pp. 342–353, Jan. 2012.

[25] M. Wang, J. Li, K. D. T. Ngo, and H. Xie, "A surface-mountable microfabricated power inductor in silicon for ultracompact power supplies," *IEEE Trans. Power Electron.*, vol. 26, no. 5, pp. 1310–1315, May 2011.

[26] J. Lee, Y.-K. Hong, S. Bae, J. Jalli, J. Park, G. S. Abo, G. W. Donohoe, and B.-C. Choi, "Integrated ferrite film inductor for power system-on-chip (PowerSoC) smart phone applications," *IEEE Trans. Magn.*, vol. 47, no. 2, pp. 304–307, Feb. 2011.

[27] Q. Li, Y. Dong, F. C. Lee, and D. Gilham, "High-Density low-profile coupled inductor design for integrated point-of-load converters," *IEEE Trans. Power Electron.*, vol. 28, no. 1, pp. 547–554, Jan. 2013.

[28] J. Qiu and C. R. Sullivan, "Inductor design for VHF tapped-inductor dc-dc power converters," in *Proc. IEEE Ind. Appl. Conf., 2012*, Mar. 6–11, 2011, pp. 142–149.

[29] C. O. Mathùna, N. Wang, S. Kulkarni, and S. Roy, "Review of integrated magnetics for power supply on chip (PwrSoC)," *IEEE Trans. Power Electron.*, vol. 27, no. 11, pp. 4799–4816, Nov. 2012.

Laili Wang (S'08–M'12) was born in Shaanxi, China, in 1982. He received the B.S., M.S., and Ph.D. degrees in electrical engineering from Xi'an Jiaotong University, Xi'an, China, in 2004, 2007, and 2011, respectively.

Since 2011, he has been a Postdoctoral Research Fellow in the Department of Electrical Engineering, Queen's University, Kingston, ON, Canada. His research interests include package and integration of passive devices in high-frequency high-power density dc/dc converters.

Zhiyuan Hu received the M.Sc. degree from the University of Ottawa, Ottawa, ON, Canada, in 2010. He is currently working toward the Ph.D. degree in electrical engineering at Queen's University, Kingston, ON, Canada.

From 2007 to 2010, he was with Potentia Semiconductor Corp. and Power Integrations Inc., in the area of reference design and IC validation for power management ICs. His research interests include resonant converters, digital control, digital communication for isolated power supplies, and power factor correction. He has one U.S. patent pending.

Mr. Hu has received conference travel awards from IAS-PELS and PSMA as a student.

Yan-Fei Liu (M'94–SM'97–F'13) received the Ph.D. degree from the Department of Electrical and Computer Engineering, Queen's University, Kingston, ON, Canada, in 1994.

From February 1994 to July 1999, he worked as a Technical Advisor with the Advanced Power System Division of Nortel Networks. Since 1999, he has been with the Queen's University, where he is currently a Professor in the Department of Electrical and Computer Engineering. His research interests include digital control technologies for high efficiency, fast dynamic response dc–dc switching converter and ac–dc converter with power factor correction, resonant converters, and server power supplies, and LED drivers. He holds 22 U.S. patents and has published more than 130 technical papers in IEEE transactions and conferences. He is also a principal contributor for two IEEE standards.

Dr. Liu has been serving as an Associate Editor for the IEEE TRANSACTIONS ON POWER ELECTRONICS since 2001, an Editor-in-Chief for Special Issue of Power Supply on Chip of IEEE TRANSACTIONS ON POWER ELECTRONICS, as well as Technical Program Cochair for ECCE 2011. He also serves as a Chair the IEEE Power Electrical Society Technical Committee on Power Conversion Systems and Components.

Yunqing Pei (M'05) was born in 1969. He received the B.S. and M.S. degrees in electrical engineering and the Ph.D. degree in power electronics all from Xi'an Jiaotong University, Xi'an, China, in 1991, 1994, and 1999, respectively.

He became a Faculty Member of Xi'an Jiaotong University. He is currently an Associate Professor at Xi'an Jiaotong University. From February 2006 to February 2007, he was a Visiting Scholar of the Center of Power Electronics Systems, Virginia Polytechnic Institute and State University. His research interests include the high-power inverters, switch mode power supply, and converters in distributed generation systems.

Xu Yang (M'02) was born in China, in 1972. He received the B.S. and Ph.D. degrees in electrical engineering from Xi'an Jiaotong University, Xi'an, China, in 1994 and 1999, respectively.

He has been a Faculty Member of the School of Electrical Engineering, Xi'an Jiaotong University since 1999, where he is currently a Professor. From November 2004 to November 2005, he was with the Center of Power Electronics Systems (CPES), Virginia Polytechnic Institute and State University, Blacksburg, as a Visiting Scholar. He then came back to Xi'an Jiaotong University, and involved in the teaching and researches in power electronics and industrial automation area. His research interests include soft switching topologies, PWM control techniques and power electronic integration, and packaging technologies.